



Contents lists available at ScienceDirect

Journal of Geochemical Exploration

journal homepage: www.elsevier.com/locate/jgeoexp

Geochemical modelling of a Zn–Pb skarn: Constraints from LA–ICP–MS analysis of fluid inclusions

Martina Bertelli^{a,*}, Timothy Baker^a, James S. Cleverley^a, Thomas Ulrich^b

^a Predictive Mineral Discovery Cooperative Research Centre and Economic Geology Research Unit, School of Earth and Environmental Science, James Cook University, Townsville, QLD 4811, Australia

^b Department of Earth & Marine Sciences, Australian National University, Canberra, ACT 0200, Australia

ARTICLE INFO

Article history:

Received 27 February 2008

Accepted 12 November 2008

Available online xxxx

Keywords:

Fluid inclusions

LA ICP MS analysis

Geochemical modelling

Zn/Pb ratios

ABSTRACT

The Bismark deposit (northern Chihuahua, Mexico) is one of several base metal-rich high-temperature, carbonate-replacement deposits hosted in northern Mexico. Previous fluid inclusion studies based on microthermometry and PIXE have shown that the Zn-rich, Pb-poor Bismark deposit formed from a moderate salinity magmatic fluid [Baker, T. and Lang, J.R., 2003. Reconciling fluid inclusion types, fluid processes, and fluid sources in skarns: an example from the Bismark Deposit, Mexico. *Mineralium Deposita* 38(4), 474–495; Baker, T., van Achterberg, E., Ryan, C.G. and Lang, J.R., 2004. Composition and evolution of ore fluids in a magmatic-hydrothermal skarn deposit. *Geology* 32(2), 117–120]. The exact precipitation mechanisms are unclear and may have due to cooling, salinity decrease and wall rock reaction. Furthermore, PIXE data suggested that Pb and Zn concentrations were comparable and inconsistent with the Zn-rich nature of the ore. However, Pb was commonly below the limit of detection for PIXE and the data presented by Baker et al. [Baker, T., van Achterberg, E., Ryan, C.G. and Lang, J.R., 2004. Composition and evolution of ore fluids in a magmatic-hydrothermal skarn deposit. *Geology* 32(2), 117–120] are regarded as the maximum concentrations of Pb in the fluid. In this study new LA ICP MS analysis was carried out on the same fluid inclusion population to compare with the PIXE data in order to constrain the uncertainty related to the Pb data and the new results are used to model possible ore deposition mechanisms. The new laser ablation data reveal overall lower concentrations of Pb in the ore fluid (average value ~285 ppm) than previously indicated by PIXE analysis (average value ~713 ppm). Chemical modelling using the new laser ablation data tested the following ore deposition processes: 1) cooling; 2) fluid–rock reaction at constant temperature; 3) cooling and simultaneous fluid–rock interaction. Modelling results show that the gangue and ore minerals observed at Bismark are best reproduced by fluid–rock interaction and simultaneous cooling. Results from the simulations strongly indicate that ore deposition was mainly driven by a pH increase due to the neutralization of the acidic ore fluid (pH=3.9) as the result of the reaction with the limestone. Modelling results also suggest that the deposit likely formed under cooling conditions, but do not support the hypothesis of a temperature decrease as the principal ore-forming process.

© 2008 Elsevier B.V. All rights reserved.

1. Introduction

Ore deposition in hydrothermal systems is the result of a complex interplay between several geochemical processes. Geochemical modelling can be used to explore the chemical effects of a wide range of processes and can aid the determination of the most likely mechanism responsible for ore formation. Any geochemical modelling exercise must be approached from an initial conceptual model which is based on well constrained field observations, data collection and a number of geological and geochemical assumptions. The validity of the model is strictly dependent on the quality and quantity of the data and on the consistency of assumptions on which the model is based. In chemical

models of geological systems one of the key areas of uncertainty is the chemical composition of the fluids that interacted with the rocks. Fluid inclusions are a sample of the fluids trapped during fluid–rock reactions, but techniques to determine their detailed chemical composition, such as Proton Induced X-ray Emission (PIXE, Ryan et al., 1991; Heinrich et al., 1992; Ryan et al., 1993, 2001) and Laser Ablation Inductively Coupled Plasma Mass Spectrometry (LA ICP MS; Gunther et al., 1998; Ulrich et al., 1999; Heinrich et al., 2003), have only recently been developed. Prior to these developments, geochemical modelling studies of fluid–rock interaction in geological systems have relied upon the assumption that the model fluid composition is controlled by equilibrium with a model rock prior to entering the system (Sverjensky, 1987; Lu et al., 1992; Komminou and Sverjensky, 1995, 1996). The latest progress of microanalytical techniques now allows in situ determination of the composition of fluid inclusions. The data from fluid inclusion analysis can now be employed to help constrain the chemical system for

* Corresponding author. School of Earth and Environmental Sciences, James Cook University, Townsville, QLD 4811, Australia.

E-mail address: martina.bertelli@jcu.edu.au (M. Bertelli).

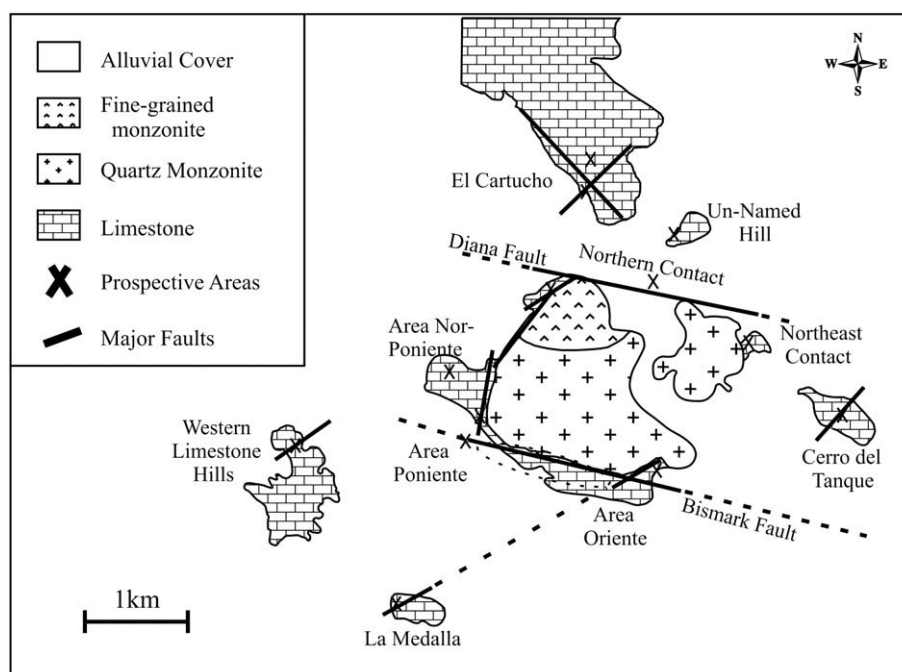


Fig. 1. Location map and geology of the Bismark deposits, Chihuahua. Modified from Baker and Lang (2003).

input into geochemical models (e.g. Heinrich et al., 2004). In this study results of numerical simulations of ore-forming processes are presented for the Bismark Zn deposit using new LA ICP MS analysis of fluid inclusions to constrain the composition of the model ore-forming fluid. The Bismark deposit is a Zn-rich skarn deposit located in the northern Chihuahua district, Mexico, and the paragenesis of the alteration and the fluid evolution history of this deposit have been described in detail by the previous studies of Baker and Lang (2003) and Baker et al. (2004). The well constrained geology together with the fluid inclusion data make this an ideal case study for geochemical modelling of an ore-forming system. Although these aspects are well constrained it is not clear which key processes led to ore precipitation. Furthermore, PIXE analysis of fluid inclusions indicate a comparable Pb and Zn concentration, in the ore fluid but the ore reserves contain 8% Zn and only 0.5% Pb. In this study new results from LA ICP MS analysis of ore stage fluid inclusions are presented and compared with the existing PIXE data (Baker et al., 2004). The comparison between the two datasets is

possible because PIXE analysis is a non-destructive technique in contrast with LA ICP MS analysis that destroys the fluid inclusion samples. The new fluid chemical data are then used as input into geochemical simulations of the potential ore forming processes.

2. Background geology and summary of previous studies

The Bismark deposit is a Zn-rich skarn located in the northern Chihuahua district, Mexico (Fig. 1). The deposit contains Zn (8%), Pb (0.5%), Cu (0.2%) and Ag (50 g/t) (Haptonstall, 1994; Baker and Lang, 2003). Rocks in the Bismark area comprise a sequence of massive to thickly-bedded Cretaceous limestones interbedded with thin layers of quartzite and shales, and intruded by a suite of Tertiary igneous rocks (~42 Ma K–Ar age on biotite, unpublished internal data of Minera Bismark S.A.) that include the Bismark stock and several dikes and sills (Fig. 1). Emplacement of the Bismark stock was controlled by the WNW-oriented Bismark and the Diana faults that border the stock on the south

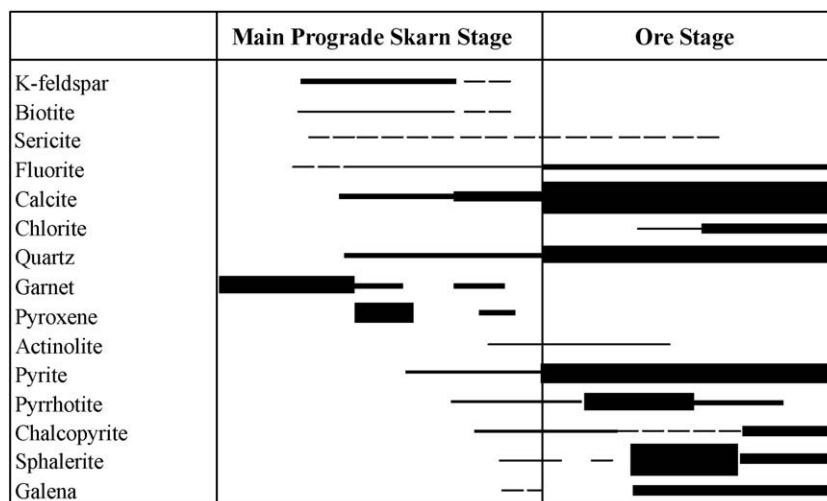


Fig. 2. Diagram showing the paragenesis of alteration within the limestone at the Bismark deposit. Width of lines indicates relative abundance. Dashed lines are minor or trace phases. Modified from Baker and Lang (2003).

Table 1

Summary of fluid inclusions characteristics of the Bismark deposit

| Type | Phases | V (vol.%) | Host | Salinity (wt.% NaCl equivalent) | Th (°C) |
|---------------------|---------------|-----------|--------------|---------------------------------|---------|
| Pre-ore brine | L–V–Hal±Syl±n | <10 | Fl, Qtz | 32–62 | 400–600 |
| Pre-ore vapour | V–L | >80 | Fl, Qtz, Cal | | |
| Syn-ore critical | L–V±op. | 40–60 | Qtz | 8.4–10.9 | 351–438 |
| Syn-ore liquid-rich | L–V±op. | 10–40 | Fl, Qtz, Cal | 5.1–11.8 | 104–336 |

Modified from Baker and Lang (2003).

and on the north respectively (Baker and Lang, 2003). The intrusion comprises a biotite-rich quartz monzonite porphyry and a minor finer-grained equivalent phase with lesser biotite (Baker and Lang, 2003).

The main ore bodies occur at the contact between the Bismark stock and the carbonate host rock along the Bismark fault. Mineralization is predominantly found as replacement of garnet-pyroxene exoskarn and limestone, in both the foot wall and the hanging wall of the Bismark fault while intrusion-hosted mineralization is rare. The paragenesis of the alteration and mineralization at the Bismark deposit is summarized in Fig. 2. Alteration of the intrusion consists of three stages that comprise early pervasive potassic (K feldspar, biotite) alteration, later fracture-controlled kaolinite alteration and a final stage of sericite-sulphide alteration. Alteration of the limestone has been subdivided in two main stages: a mostly barren prograde exoskarn that consists primarily of green-garnet of andradite-grossular composition and with quartz, calcite, fluorite, K-feldspar, pyroxene, vesuvianite and trace apatite; the final stages of the prograde skarn include the precipitation of pyrite, pyrrhotite, chalcopyrite and sphalerite. The later ore stage is composed predominantly of sphalerite, galena, pyrrhotite, pyrite, and chalcopyrite, with gangue calcite, lesser quartz, fluorite and chlorite.

Baker and Lang (2003) have recognized several populations of fluid inclusions at the Bismark deposit characterized by different temperatures and compositions (Table 1). The earliest fluid inclusion types comprise high-temperature (400 to 600 °C) halite-bearing brine (32 to

62 wt.% NaCl equivalent) coexisting with vapour inclusions (>80 vol.% vapour) found within early fluorite and predating the main ore stage. A later population of inclusions display critical to near critical behaviour and have salinity estimates ranging from 8.4 to 10.9 wt.% NaCl equivalent and homogenization temperatures between 351 and 438 °C. These inclusions were found in quartz veins associated with the mineralization and are interpreted to be samples of the ore-forming fluid (Baker et al., 2004). Finally a population of syn- to post-ore liquid-rich fluid inclusions have salinity values that range from 5.1 to 11.8 wt.% NaCl equivalent and homogenization temperatures between 104 and 336 °C. PIXE analysis on selected fluid inclusions from each population revealed that both early and ore stage fluid are charged with metals and showed that at higher temperature Zn and Pb were preferentially concentrated in the brine whereas Cu partitioned in the coexisting vapour phase (Baker et al., 2004). PIXE analysis of ore stage fluid inclusions also highlighted an apparent difference between the contents of Zn and Pb in the fluid and the ore grade of the deposit (Table 2). The analyses measured comparable concentrations of Zn and Pb, though the deposit is very Zn-rich (8%) relative to Pb (0.5%). The Pb, however, was commonly below the limit of detection for PIXE and the data presented by Baker et al. (2004) are regarded as the maximum concentrations of Pb in the fluid because the detection limits were used as a maximum estimate. New LA ICP MS analysis carried out in this study allow for lower detection limits compared to PIXE, thus constraining the uncertainty related to the Pb data.

Baker and Lang (2003) and Baker et al. (2004) inferred a common magmatic origin for both early and later fluids and interpreted their diversities as the result of the evolution of a magmatic fluid that underwent high temperature phase separation of immiscible brine and vapour, followed by the formation of later lower temperature, lower salinity ore forming fluid that formed in response to changes in temperature and pressure conditions. Similar models have been proposed for the formation of porphyry copper deposits (Shinohara and Hedenquist, 1997) and more recently also for skarns (Meinert et al., 2003). However, the process responsible for ore deposition is still unclear. Baker and Lang (2003) and Baker et al. (2004) proposed the

Table 2

PIXE analysis of ore stage low-salinity fluid inclusions from the Bismark deposit

| | | K | Ca | Fe | Mn | Zn | Cu | Pb | Cl | Zn/Pb | Zn/Cu | Pb/Cu | K/Ca | Fe/Mn | Zn/Fe |
|---------|-------------|--------|------|------|-----|------|-----|------|--------|-------|-------|-------|------|-------|-------|
| 3 | Conc. (ppm) | 5277 | 2995 | 400 | 395 | 198 | 94 | 402 | 12,289 | 0.5 | 2.1 | 4.3 | 1.8 | 1.0 | 0.5 |
| | 1σ s.d. | 9754 | 1764 | 405 | 91 | 439 | 141 | 374 | 29,237 | | | | | | |
| | LOD (ppm) | 163 | 119 | 51 | 60 | 56 | 60 | 459 | 466 | | | | | | |
| 5 | Conc. (ppm) | 22,776 | 2813 | 559 | 200 | 395 | 349 | 954 | 56,698 | 0.4 | 1.1 | 2.7 | 8.1 | 2.8 | 0.7 |
| | 1σ s.d. | 9754 | 1764 | 405 | 91 | 439 | 141 | 374 | 29,237 | | | | | | |
| | LOD (ppm) | 192 | 160 | 95 | 109 | 110 | 118 | 954 | 348 | | | | | | |
| 7 | Conc. (ppm) | 31,408 | 4206 | 588 | 247 | 479 | 474 | 935 | 94,672 | 0.5 | 1.0 | 2.0 | 7.5 | 2.4 | 0.8 |
| | 1σ s.d. | 9754 | 1764 | 405 | 91 | 439 | 141 | 374 | 29,237 | | | | | | |
| | LOD (ppm) | 235 | 185 | 97 | 112 | 109 | 115 | 935 | 531 | | | | | | |
| 8 | Conc. (ppm) | 7405 | 2348 | 270 | 103 | 286 | 200 | 862 | 20,795 | 0.3 | 1.4 | 4.3 | 3.2 | 2.6 | 1.1 |
| | 1σ s.d. | 9754 | 1764 | 405 | 91 | 439 | 141 | 374 | 29,237 | | | | | | |
| | LOD (ppm) | 183 | 153 | 90 | 103 | 104 | 110 | 862 | 316 | | | | | | |
| 9 | Conc. (ppm) | 16513 | 7151 | 1554 | 263 | 1605 | 336 | 1547 | 56,296 | 1.0 | 4.8 | 4.6 | 2.3 | 5.9 | 1.0 |
| | 1σ s.d. | 9754 | 1764 | 405 | 91 | 439 | 141 | 374 | 29,237 | | | | | | |
| | LOD (ppm) | 1142 | 674 | 184 | 209 | 185 | 205 | 1547 | 6962 | | | | | | |
| 12 | Conc. (ppm) | 2070 | 865 | 147 | 138 | 46 | 104 | 465 | 4831 | 0.1 | 0.4 | 4.5 | 2.4 | 1.1 | 0.3 |
| | 1σ s.d. | 9754 | 1764 | 405 | 91 | 439 | 141 | 374 | 29,237 | | | | | | |
| | LOD (ppm) | 270 | 171 | 51 | 62 | 55 | 59 | 465 | 1267 | | | | | | |
| 14 | Conc. (ppm) | 2540 | 3196 | 432 | 164 | 369 | 56 | 402 | 7568 | 0.9 | 6.6 | 7.2 | 0.8 | 2.6 | 0.9 |
| | 1σ s.d. | 9754 | 1764 | 405 | 91 | 439 | 141 | 374 | 29,237 | | | | | | |
| | LOD (ppm) | 202 | 135 | 48 | 57 | 52 | 55 | 402 | 770 | | | | | | |
| 15 | Conc. (ppm) | 5926 | 2685 | 518 | 102 | 441 | 122 | 332 | 16,026 | 1.3 | 3.6 | 2.7 | 2.2 | 5.1 | 0.9 |
| | 1σ s.d. | 9754 | 1764 | 405 | 91 | 439 | 141 | 374 | 29,237 | | | | | | |
| | LOD (ppm) | 172 | 123 | 41 | 48 | 44 | 47 | 307 | 663 | | | | | | |
| 16 | Conc. (ppm) | 4069 | 961 | 96 | 115 | 76 | 73 | 522 | 10,353 | 0.1 | 1.0 | 7.2 | 4.2 | 0.8 | 0.8 |
| | 1σ s.d. | 9754 | 1764 | 405 | 91 | 439 | 141 | 374 | 29,237 | | | | | | |
| | LOD (ppm) | 315 | 198 | 57 | 69 | 63 | 64 | 522 | 1494 | | | | | | |
| Average | | 10,887 | 3024 | 507 | 192 | 433 | 201 | 713 | 31,059 | 0.6 | 2.5 | 4.4 | 3.6 | 2.7 | 0.8 |

Numbers printed in italic refer to values that are below the detection limits. Conc. = concentration; LOD = limit of detection.

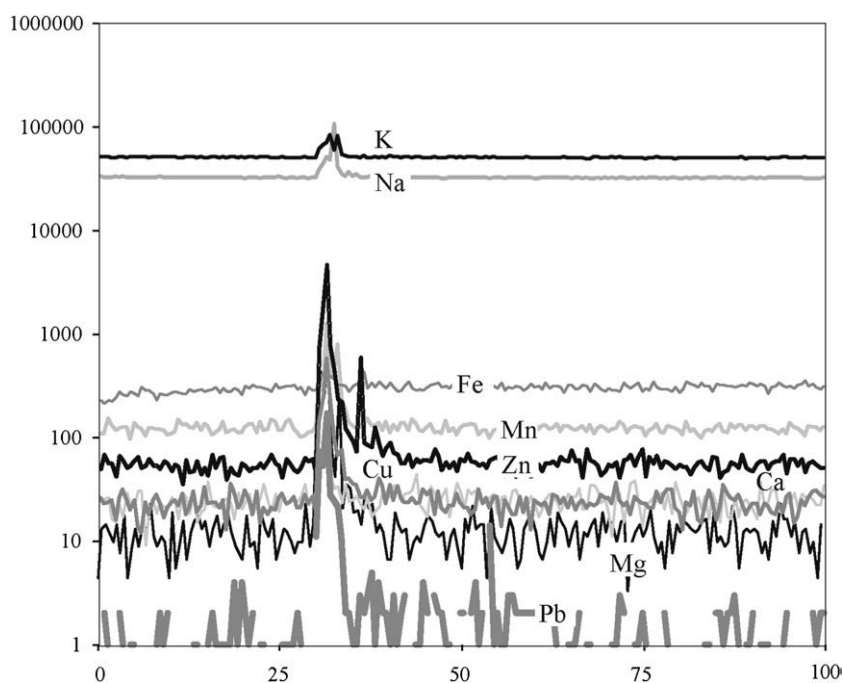


Fig. 3. Typical LA ICP MS signal from a single fluid inclusion (fluid inclusion 53) from the Bismark deposit (Mexico).

following possible ore deposition mechanisms: temperature decrease, salinity decrease, pressure decrease and reaction of the ore-forming fluid with the host rock. The purpose of this paper is therefore to test ore deposition processes using geochemical modelling and new ore stage fluid inclusion data to constrain the initial composition of the fluid used in the simulations. Initial pressures and temperatures of 200 bars and 350 °C were used in the modelling based on results from

microthermometric analysis of the ore stage fluid inclusions (Baker and Lang, 2003).

3. LA ICP MS analysis of fluid inclusions

The chemistry of ore-stage fluid inclusions from the Bismark deposit was determined by LA ICP MS analysis undertaken at the

Table 3

LA ICP MS analysis of ore stage low-salinity fluid inclusions from the Bismark deposit

| | | K | Ca | Mg | Fe | Zn | Cu | Mn | Pb | Ag | Zn/Pb | Zn/Cu | Pb/Cu | K/Ca | Fe/Mn | Zn/Fe |
|---------|-------------|---------|--------|------|--------|------|------|-----|-----|------|-------|-------|-------|------|-------|-------|
| 5 | Conc. (ppm) | 36,340 | 7884 | 1444 | 1184 | 1454 | 703 | 249 | 206 | 3.47 | 7.1 | 2.1 | 0.3 | 4.6 | 4.8 | 1.2 |
| | 1σ s.d. | 20,447 | 7248 | 734 | 6804 | 2170 | 194 | 99 | 67 | 2 | | | | | | |
| | LOD (ppm) | 377 | 1208 | 3 | 252 | 8 | 6 | 3 | 2 | 0 | | | | | | |
| 7 | Conc. (ppm) | 41,983 | 7575 | 467 | 1070 | 583 | 413 | 323 | 188 | 3.15 | 3.1 | 1.4 | 0.5 | 5.5 | 3.3 | 0.5 |
| | 1σ s.d. | 20,447 | 7248 | 734 | 6804 | 2170 | 194 | 99 | 67 | 2 | | | | | | |
| | LOD (ppm) | 227 | 1392 | 4 | 271 | 6 | 4 | 3 | 2 | 0 | | | | | | |
| 6 | Conc. (ppm) | 37,191 | 22,109 | 439 | 5124 | 3168 | 743 | 419 | 285 | 8.98 | 11.1 | 4.3 | 0.4 | 1.7 | 12.2 | 0.6 |
| | 1σ s.d. | 20,447 | 7248 | 734 | 6804 | 2170 | 194 | 99 | 67 | 2 | | | | | | |
| | LOD (ppm) | 3739 | 19,173 | 50 | 3179 | 75 | 66 | 55 | 18 | 4 | | | | | | |
| 8 | Conc. (ppm) | 54,951 | 12,372 | 2670 | 2767 | 2638 | 734 | 120 | 368 | 2.11 | 7.2 | 3.6 | 0.5 | 4.4 | 23.1 | 1 |
| | 1σ s.d. | 20,447 | 7248 | 734 | 6804 | 2170 | 194 | 99 | 67 | 2 | | | | | | |
| | LOD (ppm) | 1045 | 6973 | 24 | 1046 | 23 | 17 | 15 | 9 | 1 | | | | | | |
| 52 | Conc. (ppm) | 32,180 | 11,649 | 965 | 25,482 | 3303 | 705 | 254 | 282 | 3.25 | 11.7 | 4.7 | 0.4 | 2.8 | 100.3 | 0.1 |
| | 1σ s.d. | 20,447 | 7248 | 734 | 6804 | 2170 | 194 | 99 | 67 | 2 | | | | | | |
| | LOD (ppm) | 379 | 3022 | 8 | 591 | 15 | 14 | 7 | 3 | 1 | | | | | | |
| 53 | Conc. (ppm) | 22,998 | 21,581 | 849 | 3269 | 2501 | 564 | 353 | 221 | 1.41 | 11.3 | 4.4 | 0.4 | 1.1 | 9.3 | 0.8 |
| | 1σ s.d. | 20,447 | 7248 | 734 | 6804 | 2170 | 194 | 99 | 67 | 2 | | | | | | |
| | LOD (ppm) | 623 | 6214 | 21 | 896 | 18 | 24 | 12 | 5 | 2 | | | | | | |
| 60 A | Conc. (ppm) | 38,009 | 7011 | 2253 | 7871 | 6630 | 356 | 338 | 377 | 3.27 | 17.6 | 18.6 | 1.1 | 5.4 | 23.3 | 0.8 |
| | 1σ s.d. | 20,447 | 7248 | 734 | 6804 | 2170 | 194 | 99 | 67 | 2 | | | | | | |
| | LOD (ppm) | 1185 | 7011 | 22 | 1071 | 28 | 33 | 23 | 9 | 1 | | | | | | |
| 60 B | Conc. (ppm) | 35,170 | 18,548 | 756 | 10,188 | 8211 | 712 | 151 | 300 | 1.42 | 27.4 | 11.5 | 0.4 | 1.9 | 67.6 | 0.8 |
| | 1σ s.d. | 20,447 | 7248 | 734 | 6804 | 2170 | 194 | 99 | 67 | 2 | | | | | | |
| | LOD (ppm) | 2873 | 17,102 | 54 | 2590 | 69 | 82 | 55 | 22 | 3 | | | | | | |
| 61 | Conc. (ppm) | 101,083 | 29,286 | 1624 | 6808 | 4112 | 716 | 267 | 375 | 6.68 | 11 | 5.7 | 0.5 | 3.5 | 25.5 | 0.6 |
| | 1σ s.d. | 20,447 | 7248 | 734 | 6804 | 2170 | 194 | 99 | 67 | 2 | | | | | | |
| | LOD (ppm) | 1308 | 4831 | 15 | 832 | 15 | 22 | 14 | 6 | 1 | | | | | | |
| 62 | Conc. (ppm) | 44,961 | 20,926 | 1970 | 4483 | 3078 | 1100 | 441 | 249 | 6.49 | 12.4 | 2.8 | 0.2 | 2.1 | 10.2 | 0.7 |
| | 1σ s.d. | 20,447 | 7248 | 734 | 6804 | 2170 | 194 | 99 | 67 | 2 | | | | | | |
| | LOD (ppm) | 918 | 5500 | 13 | 786 | 14 | 25 | 13 | 7 | 1 | | | | | | |
| Average | | 44,487 | 15,894 | 1344 | 6825 | 3568 | 675 | 292 | 285 | 4 | 12 | 5.9 | 0.5 | 3.3 | 28.0 | 0.7 |

Values in ppm. Numbers printed in italic refer to values that are below the detection limits.

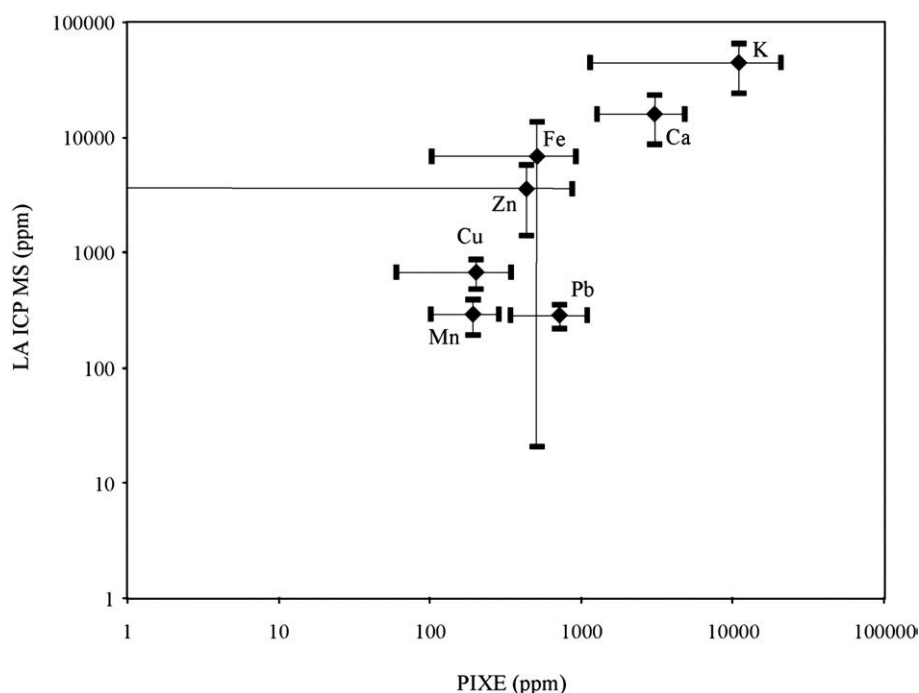


Fig. 4. Element concentrations determined by LA ICP MS plotted against PIXE analyses. Error bars indicate 1σ of the variability within one assemblage.

facilities of Research School of Earth Sciences of the Australian National University. The instrumentation employed combines a 193 nm excimer laser (Lambda Physik, Germany) to open the inclusion and volatilize its content, and an Agilent 7500 s ICPMS which analyzes the ablated material (Gunther et al., 1998; Heinrich et al., 2003). The ICP MS quadrupole instrumentation records transient signals in succession, by cycling through all masses of interest and measuring each for a short period (the 'dwell time') (Heinrich et al., 2003). For the analysis of the Bismark fluid inclusions the dwell time was 20 ms for each isotope and the dead time between measurements from one isotope to the next was 40 ns. A total of 23 elements were analysed and the time to complete a sampling cycle was 0.512 s. Therefore, every mass was analysed approximately every 0.5 s. The signal duration for each measured fluid inclusion spanned from 3 to 5.6 s. Fig. 3 shows a typical signal for a single fluid inclusion from the Bismark deposit. The technique provides multi-element analysis and quantitative measurement of element ratios. The value of Na determined from microthermometry (3.7 wt.%, average composition of ore stage fluid inclusions at Bismark; Baker and Lang, 2003) was used as internal standard to convert the element ratios to absolute concentrations (Gunther et al., 1998; Heinrich et al., 2003). Analytical precision using Na as an internal standard is typically within 20% (Gunther et al., 1998; Heinrich et al., 2003). Detection limits are highly variable and must be determined for each element in each inclusion because they are a function of the mass of the element, the size and shape of the inclusion, the number of elements measured from a single inclusion and the opening procedure (Gunther et al., 1998; Heinrich et al., 2003). Detection limits for the Bismark fluid inclusions are reported in Table 3. Uncertainties and their potential sources are further discussed in Section 4.

A total of 10 low salinity ore stage fluid inclusions were analysed, all from the same sample of syn-ore quartz vein (Table 3). Here results are presented only for the elements that we used in our modelling simulations: K, Ca, Fe, Mg, Mn, Zn, Cu, Pb and Ag (Table 3, Fig. 4). The data reveal high concentrations of K and Ca ranging from about 23,000 to approximately 100,000 ppm and from around 7000 to about 29,000 ppm respectively. Magnesium content in the fluid varies from approximately 400 ppm to around 3000 ppm. The fluid carries a considerable concentration of metals: Fe and Zn are

particularly enriched in the fluid, displaying average concentrations higher than 1000 ppm while Cu, Pb and Ag concentrations are generally lower than 1000 ppm. Manganese concentrations range from 120 to 441 ppm.

4. Comparison of LA ICP MS and PIXE data

In this section results obtained from PIXE analysis by (Baker et al., 2004) are compared with laser ablation analysis of ore stage fluid inclusions measured in this study. The discussion is restricted to elements measured with both techniques. The comparison of the two datasets shows that absolute element concentrations measured by the PIXE method are consistently lower than those obtained from laser ablation for all the elements except Pb and Mn (Fig. 4). The systematic error between the two datasets (excluding Pb and Mn) likely reflects the different quantification processes employed by the two techniques (Ryan et al., 1991; Heinrich et al., 1992; Ryan et al., 1993; Ryan et al., 2001; Heinrich et al., 2003). Quantification of PIXE analysis requires modelling of the fluid inclusion geometry and estimation of depth and thickness all of which may result in significant errors (up to 30%; Heinrich et al., 1992). Geometry related errors result from the deviation of the actual inclusion shape to that of a modelled ellipse (Ryan et al., 1991; Heinrich et al., 1992). Depth in particular affects the determination of concentrations of light elements due to absorption of low-energy X-rays (K lines for $Z < 21$ and L lines for $Z < 50$) producing, for example, errors of more than 50 percent in Cl concentrations for depth uncertainty of $\pm 1.5 \mu\text{m}$ (Heinrich et al., 1992). However, high-energy X-rays (K lines $Z > 25$ and L lines $Z > 60$) are less sensitive to depth. Uncertainties in the thickness of the inclusion create errors in the estimation of their volume that may produce an approximate proportional error in the element concentrations (Ryan et al., 1991). Heterogeneities in the inclusion, such as the presence of vapour and/or daughter phases represent additional sources of error in the element concentrations due to variations in X-ray absorption and variations in beam intensity for different vapour bubble and/or crystal position (Ryan et al., 1991; Heinrich et al., 1992).

By comparison LA ICP MS does not suffer depth-related or inclusion size and geometry problems as much as PIXE (Heinrich et al.,

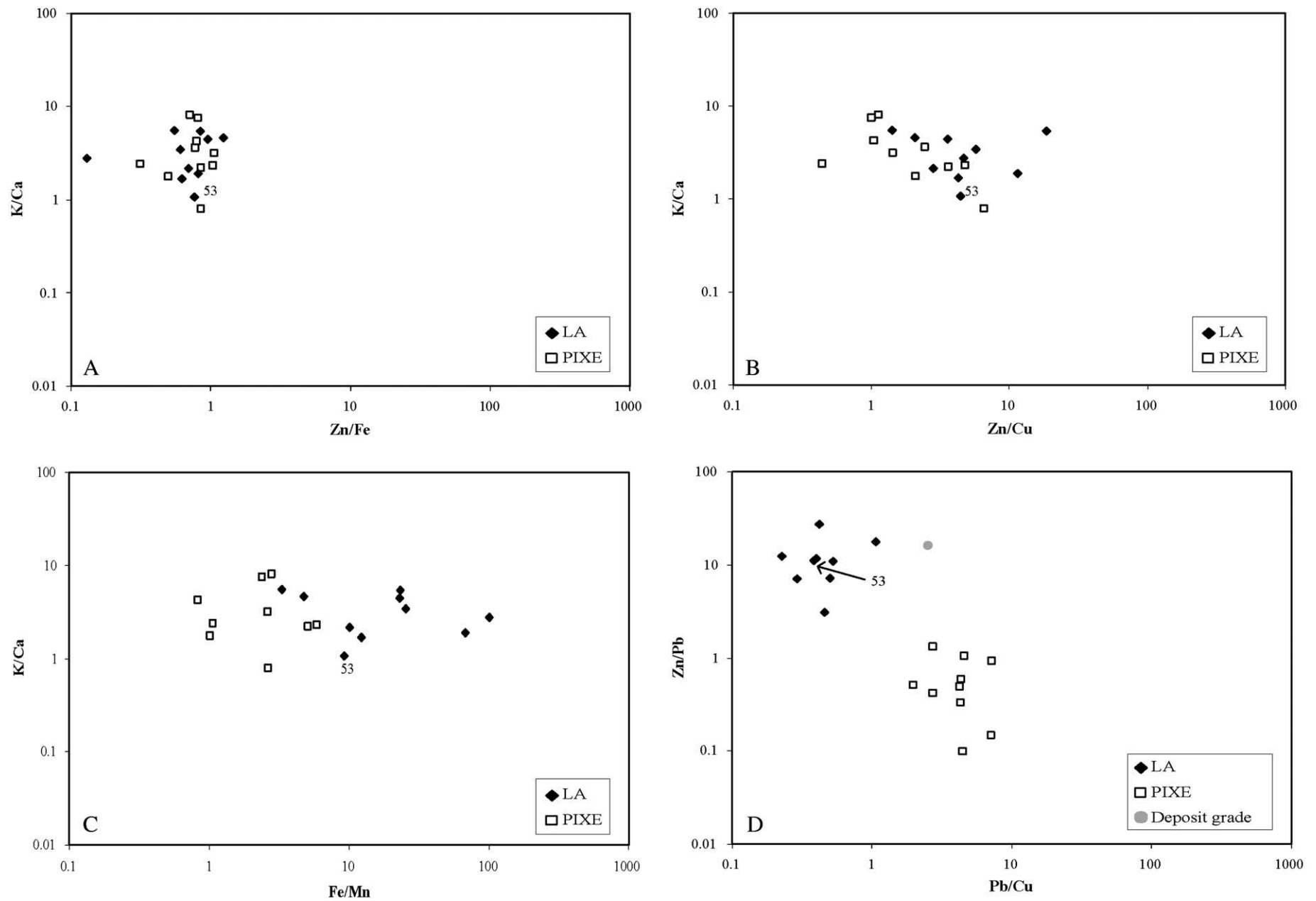


Fig. 5. Scatter plot illustrating the inter-element ratio variation between PIXE and LA ICP MS. K, Ca, Fe and Zn correlate well between the two techniques (A), whereas ratio plots including Pb and Mn have a poor correlation (B, C and D). D also illustrates that the metal ratios from LA ICP MS are more consistent with the deposit ore grade ratio. Fluid inclusion 53 was chosen to constrain the initial fluid composition used in the modelling simulations.

2003; Allan et al., 2005). Detection limits do depend on the inclusion size, that controls the overall signal duration, but the detection limits are typically significantly lower than PIXE (ppm to ppb compared with tens of ppm respectively; Ryan et al., 1991; Heinrich et al., 1992; Ryan et al., 1993, 2001; Heinrich et al., 2003; Allan et al., 2005). Large fluid inclusions allow for longer sampling time compared to small inclusions resulting in longer but lower signals (Gunther et al., 1998), allowing a greater number of measurements on each element over the duration of the signal and, therefore, potentially providing more representative and reproducible analysis (Heinrich et al., 2003). However, for heterogeneous fluid inclusions enclosing a daughter crystal, the integration of the entire signal may lead to a dilution of those elements contained in the daughter phase (the intensity for these elements may be high but for a short period of time compared to the total length of the signal) producing a consequent deterioration of detection limits (Gunther et al., 1998). These problems unlikely influenced the analysis of the Bismark fluid inclusions that were small and, thus, provided short signals. Shorter and higher intensity signals generally provide improved detection limits but poorer representative sampling due to the reduced number of measurements for each element, possibly leading to less reproducible analyses (Heinrich et al., 2003). Heinrich et al. (2003) defined a minimum duration for the transient signal (a few seconds) and a minimum number of sampling cycles (10 to 15 with 10 ms dwell time for each element) to obtain meaningful analysis and avoid systematic errors. Signal durations for the Bismark fluid inclusions vary from 3 to 5.6 allowing for 6 to 11 sampling cycles with 20 ms dwell time for each element. Therefore, each element was analysed for a minimum of 120 ms, thus, complying with the above requirements. Accurate LA ICP MS results rely on sampling and subsequent transport and detection of a representative amount of the analysed material (Heinrich et al., 2003). Imperfect sampling and the possibility of losing material, in particular small daughter minerals, during ablation and/or transport represent a weakness of LA ICP MS analysis and may result in large errors. Loss of material and subsequent elemental fractionation may occur at the ablation spot, supposedly due to partial recondensation of analyte melt onto the ablation surface and the crater walls (Eggins et al., 1998; Heinrich et al., 2003), or in the inductively coupled plasma, due to incomplete ionization and volatilization of the sample particles (Heinrich et al., 2003). Recent work have shown that these types of elemental fractionations are sensibly reduced by the reduction of the laser wavelength with best results obtained employing excimer lasers with 193 nm (Eggins et al., 1998; Gunther and Heinrich, 1999; Horn et al., 2000; Guillon and Gunther, 2002; Heinrich et al., 2003) such as the laser used for the analysis of the Bismark fluid inclusions. Imperfect ablation of inclusions, especially of those containing daughter phases, can be an additional problem and care needs to be taken when selecting an internal standard (Heinrich et al., 2003). In this case, Na was chosen and a value of 37,400 ppm was applied to convert element ratios obtained from the analysis to absolute element concentrations. This corresponds to ~9.6 wt. % NaCl equivalent which is the average salinity of the inclusions determined from microthermometry (Baker and Lang, 2003). The total salinity range for the inclusions varies from 8.4 to 10.9 wt.% NaCl equivalent (~33,000 to 43,000 ppm Na). The maximum and minimum Na values were used to recalculate the absolute element concentrations, and resulted in maximum absolute concentration increasing by an average of ~15% and minimum absolute concentrations reduced by an average of ~12%. Additional problems may arise in case too much material surrounding the fluid inclusions is ablated. The problem in relation to the present analysis is discussed below. Further explanation for the different concentrations measured by the two techniques may be found in the natural variability that characterizes fluid inclusions even within the same populations (observed by an order of magnitude variation in almost the entire suite of element concentrations measured), however, this is unlikely to result in systematic differences between the two

techniques in this case where the same inclusion populations, and indeed some of the same inclusions, have been analyzed.

In order to remove the effects of the quantification procedures, and assess how well the two data sets compare, element ratios were calculated (Tables 2 and 3) and plotted on X–Y scatter plots (Fig. 5). The results show excellent correlation between the two datasets for inter-element ratios that include K, Ca, Zn and to a lesser extent Fe, Mn and Cu, however, comparison of ratios that use Pb is poor. Lead PIXE data are mostly below detection limits, shown in italics in Table 2 and considered a maximum concentration estimate. Fe/Mn ratios from laser ablation are generally higher and display larger variations compared with PIXE Fe/Mn ratios (Fig. 5C). Fe/Mn ratios from laser ablation mostly span within one order of magnitude similarly to Fe/Mn data from PIXE, and display good correlation with PIXE Fe/Mn data, with few values displaying larger variation that appears to be linked to Fe scattering and, in particular, to few high values. In contrast, Mn from LA ICP MS values does not vary significantly in the analysed fluid inclusions. Several factors may be invoked to explain Fe high values. Analytical errors due to potential loss of material can be excluded since only successfully ablated fluid inclusions were considered. Furthermore, signals were checked and spikes were removed. Accidental ablation of a tiny opaque solid phase proximal to the analysed inclusion may explain the Fe scattering. However, to avoid contamination only fluid inclusions isolated from other inclusions or solid inclusions were selected for analysis and particular care was taken during the ablation procedure to try to avoid ablating too much of the material surrounding the fluid inclusions. Moreover, a solid inclusion would have needed to be at the exact same depth as the fluid inclusion, otherwise it would have appeared as a separate signal before or after the fluid inclusion signal, and, although possible, it appears highly unlikely. Alternatively, the Fe variation may be attributed to very small opaque daughter phases that might have been present in some inclusions but absent in others. Opaque daughter minerals were not observed in the analysed inclusions but were reported in fluid inclusions of the same type (Baker and Lang, 2003). Therefore, it is possible that few inclusions with high Fe values (e.g. fluid inclusion 52) did in fact contain tiny not visible Fe-bearing daughter phases. Unfortunately, these particular fluid inclusions were not analysed by PIXE analysis that might have confirmed the presence of a daughter phase. The possibility of a small daughter phase being analysed may result in an additional problem due to the ICP setting of analysing elements sequentially. The measuring time of a small daughter phase is obviously reduced, depending on how long that signal lasts and in which scanning position the mass spectrometer sits when the daughter phase is sampled. The scanning goes from low mass to high mass and subsequently starts again at the low mass end. Therefore, if the daughter phase is sampled while the scanning is somewhere on an element with middle mass, then there would be less measuring time on the low mass end. The switching from one isotope to another may indeed lead to less accurate and reproducible results if the fluid inclusions contain a small daughter mineral, resulting, for example in very high counts for some elements in some fluid inclusions. However, it would be expected that this problem would affect not only Fe but randomly all the other analysed elements that instead do not display significant variations (Table 3, Fig. 4). Furthermore, this problem would be limited only to fluid inclusions actually containing a small daughter phase as it appears impractical that all the analysed inclusions contained a daughter phase that is effectively not visible. Only three inclusions were analyzed with both methods (indicated as 5, 7 and 8) and PIXE did not detect daughter minerals. Overall there is a good correlation between most of the Fe/Mn ratios determined by PIXE and LA, with some high Fe/Mn values from LA linked to high Fe concentrations possibly related to the presence of daughter minerals in a small number of inclusions.

In summary, each technique has its own strength and weaknesses so that the choice of the method to employ depends on the scope of

Table 4

Input data used to constrain the initial fluid composition of the fluid used for simulation of ore-forming processes

| Elements | | |
|---|-------------------------------|---------|
| <i>Analyzed (ppm)</i> | | |
| K+ | From LA analysis | 22,998 |
| Ca++ | " | 21,581 |
| Mg++ | " | 849 |
| Mn++ | " | 353 |
| Fe++ | " | 4500 |
| Zn++ | " | 2501 |
| Pb++ | " | 221 |
| Ag+ | " | 3.3 |
| Cl- | From microthermometry | 58,000 |
| Na+ | " | 37,400 |
| <i>Calculated at 350 °C and 200 bar (ppm)</i> | | |
| H ₂ S(aq) | Equilibrium with pyrrhotite | 2952 |
| SiO ₂ (aq) | Equilibrium with quartz | 618 |
| Al+++ | Equilibrium with kfeldspar | 18.7 |
| Cu+ | Equilibrium with chalcopyrite | 34.8 |
| F- | Equilibrium with fluorite | 111 |
| pH | | 3.9 |
| logfO ₂ | | -31.019 |
| CO ₂ (aq) | | 440 |

the analysis and on the fluid inclusion material to analyze. The combination of both methods allows for a more detailed data analysis. However, it seems that overall the laser ablation data, with much lower detection limits than PIXE, provide a better estimate of the fluid compositions at the Bismark deposit. This is apparent when considering the ore grade ratios for Zn, Pb and Cu that have a better correlation with the laser ablation data than PIXE due mainly to PIXE inability to accurately measure Pb concentration (Fig. 5D). Lead PIXE values are in fact mostly below detection limit and the reported values represent a maximum estimate of the true Pb concentration in the fluid. As a consequence, PIXE Zn/Pb and Pb/Cu ratios represent respectively an underestimate and overestimate of the true Zn/Pb and Pb/Cu ratios in the fluid that are better represented by LA ICP MS values.

An important purpose of comparing the data was to select a reliable single analysis to apply to the modelling of ore-forming processes for the Bismark deposit. The LA data were selected for the modelling experiment because of the low detection limits for Pb and the fact that most of the other elements appear to be proportionally similar between the two analytical methods. In particular, inclusion 53 was chosen to constrain the initial fluid composition because of the good overlapping displayed between the two sets of data (Fig. 5).

5. Geochemical modelling

5.1. Overview of the method

Thermodynamic calculations were carried out using the program React included in The Geochemists Workbench (GWB) software package (Bethke, 1996, 2002). React can model equilibrium states and chemical reactions of systems involving an aqueous phase, minerals and gases. React was used to determine the initial composition of the fluid for the simulations and to run simulations of ore-forming processes. The thermodynamic dataset used was specifically created for this study case to fit the T–P conditions (350 °C, 200 bars) at which the deposit is thought to have formed. These are higher than the T–P working conditions of GWB default datafiles (temperatures up to 300 °C and pressures along the curve of water). The source of thermodynamic data was the Geoscience Australia version of the UNITERM database (Bastrakov, 2003), a utility database included in HCh software package (Shvarov and Bastrakov, 1999), consistent with the freeGs database (Bastrakov et al., 2004). Within the UNITERM database, the selected thermodynamic data for the majority of aluminosilicates and for carbonates were compiled by Berman (1988). The

rest of the mineral data as well as data for aqueous species were taken from a modified SUPCRT database (Pokrovskii et al., 1998). The file containing the thermodynamic data was then adapted to the GWB environment using utilities developed by Cleverley and Bastrakov (2005). Activity coefficients for aqueous species are calculated based on method described by Helgeson (1969).

5.2. Fluid composition

The ore fluid composition used in the simulations was reconstructed utilizing the laser ablation data of the low salinity inclusions at Bismark and from phase equilibria relationships. It was assumed that the fluid was in equilibrium with the late main skarn mineral assemblage consisting of quartz, pyrite, fluorite, pyrrhotite, chalcopyrite, muscovite and minor sphalerite (Fig. 2). The pre-ore assemblage also includes calcite, which, however, is not ubiquitous throughout the deposit. The fluid was not set in equilibrium with calcite in the assumption that the fluid had not reacted enough with the rock to be in equilibrium with calcite. Here the steps followed to define the fluid composition are summarized (Table 4):

1. Element concentrations of Ca, K, Fe, Zn, Pb, Mg, Mn, and Ag were taken from the laser ablation data of fluid inclusion 53. The concentration of Fe was set to a slightly higher value (4500 ppm) than the one of the inclusion (3269 ppm) to allow for the coexistence of pyrrhotite and pyrite which occur together in the deposit mineral assemblage.
2. Pyrite, quartz, fluorite, chalcopyrite and K-feldspar were used to constrain the amount of total sulphur, SiO₂(aq), F, Cu and Al respectively. Copper was constrained by setting chalcopyrite in the initial system in order to increase the amount of total sulphur and allow the simultaneous equilibrium of pyrite, chalcopyrite and pyrrhotite.
3. Temperature (350 °C), pressure (200 bar), Na (37,000 ppm) and Cl (58,000 ppm) contents were defined by microthermometric studies (Baker and Lang, 2003).
4. CO₂ was set equal to 0.01 molality unit, based on previous studies on a similar skarn system (Lu et al., 1992), because no data on CO₂ content was available from Bismark.
5. Oxygen fugacity was calculated based on the assumption of the coexistence of pyrrhotite and pyrite at the conditions of the model.
6. The pH value was set at 4 that provides equilibrium with muscovite.

The equilibrium fluid was saturated with quartz, pyrite, sphalerite, pyrite, pyrrhotite, chalcopyrite, and muscovite. The concentration of major elements largely reflects the element concentrations set initially to constrain the system; Zn concentration in the final fluid (2000 ppm) is slightly less than in the fluid inclusion (2501 ppm). Copper concentration in the final fluid (36 ppm) is one order of magnitude less than in the fluid inclusion (564 ppm). However, this latter value was obtained by setting chalcopyrite for Cu in the initial system and not the inclusion content. Attempts at setting copper concentrations in the initial system invariably lead to low copper concentrations in the final fluid, suggesting that Cu has probably low solubility in such fluid conditions. The final oxidation state (logfO₂ = -31.019) and pH (3.9) of the fluid does not vary significantly from the input data (logfO₂ = -31.3 and pH = 4). Data relative to the distribution of aqueous species for Zn, Pb, Cu and Fe show that these elements are transported mainly as chloride complexes.

5.3. Process modelling

The first model tested is an example of a polythermal path model that in our case consists of a temperature decrease from 350 °C to 100 °C at a constant rate through a series of steps; at the end of each step the program calculates the new equilibrium state of the system. The second model tested the reaction of the ore fluid with the host

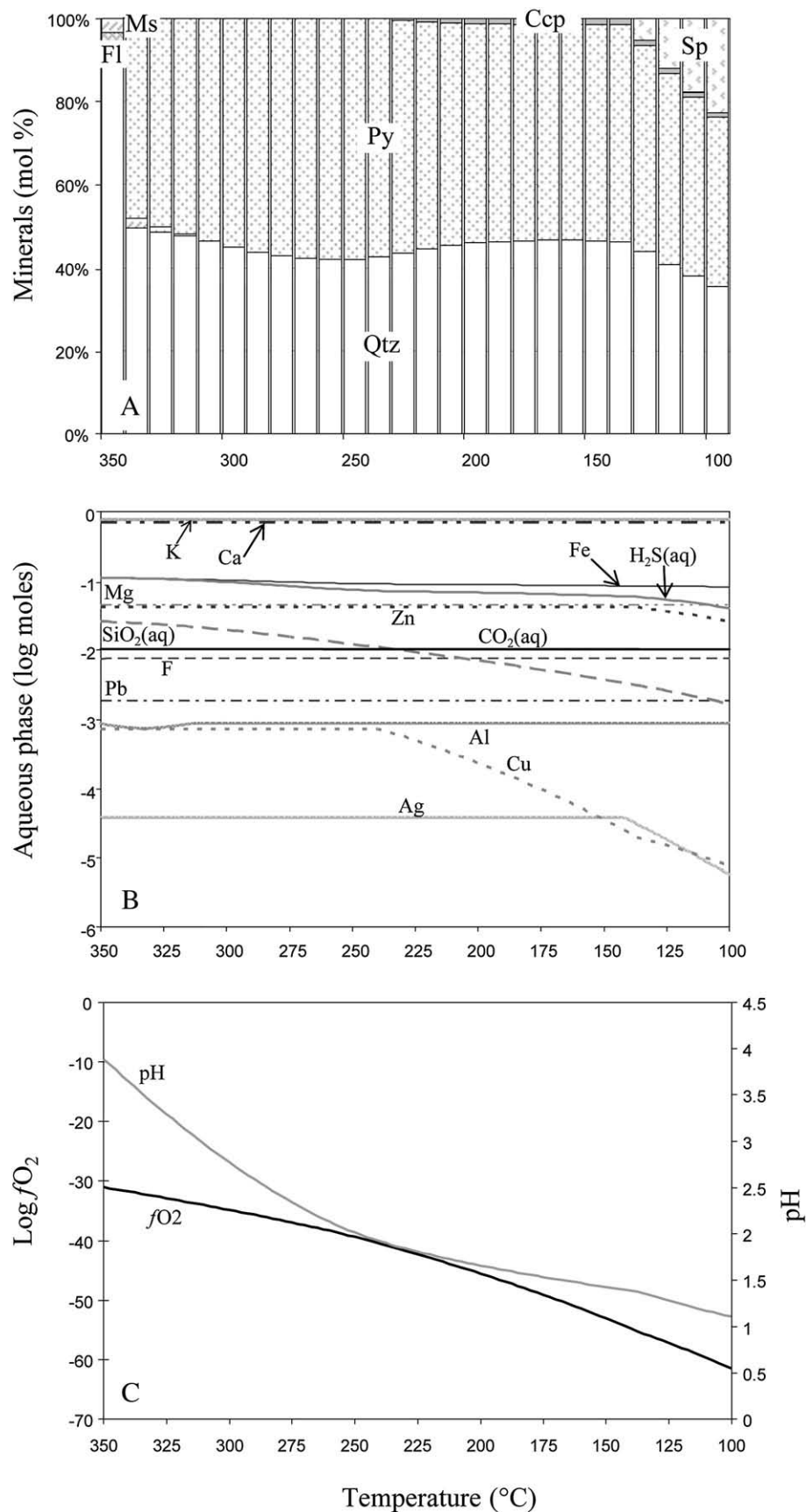


Fig. 6. Mineral assemblages, composition of the aqueous phase and gases resulting from cooling the ore fluid from 350 °C to 100 °C. (A) Alteration and ore mineral assemblages (the acanthite concentration was very low and cannot be visualized); (B) Total element concentrations; (C) pH and oxygen fugacity. Mineral abbreviation after Kretz (1983): chalcopyrite (ccp), fluorite (fl), muscovite (ms), quartz (qtz), pyrite (py), sphalerite (sp).

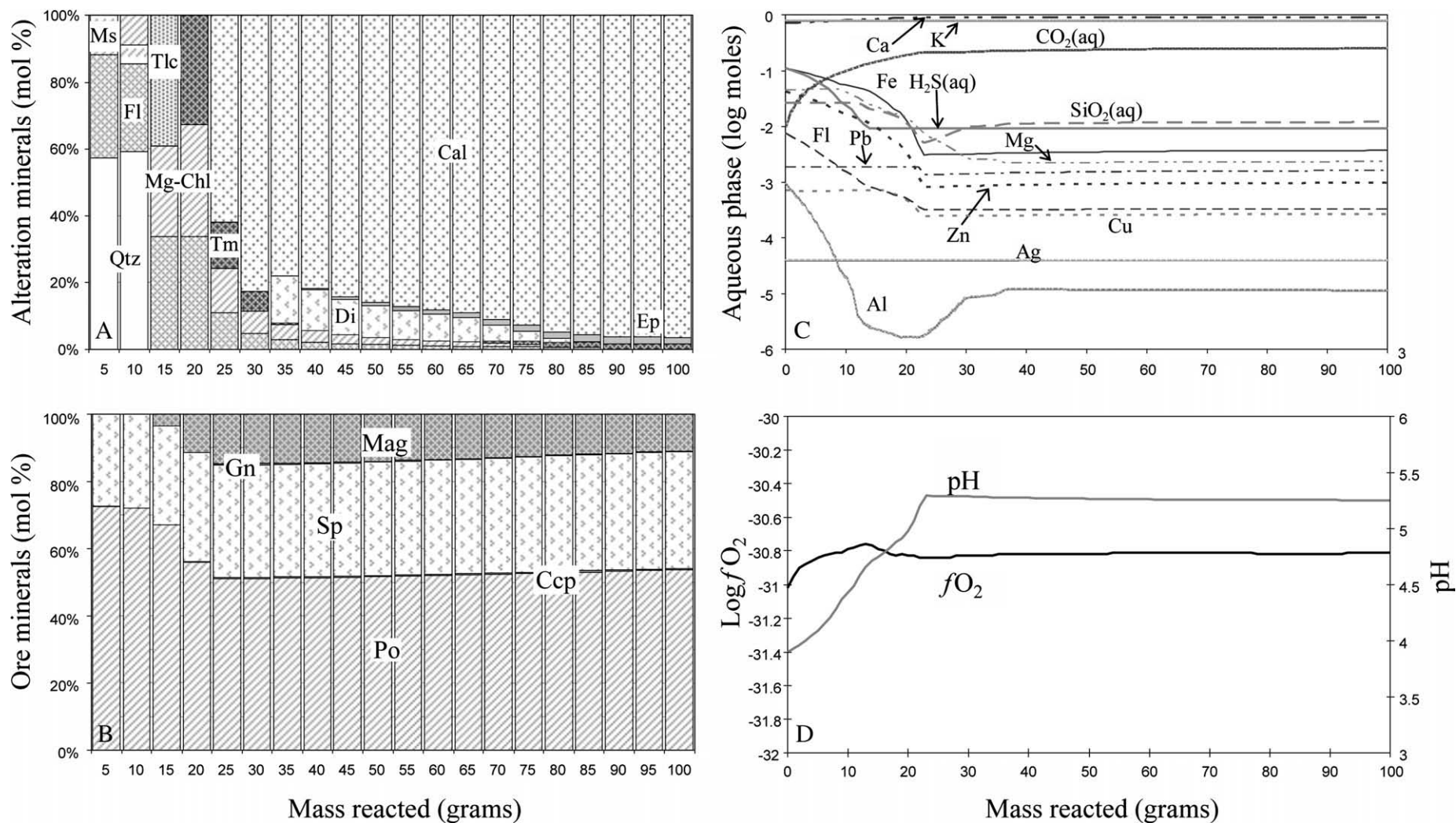


Fig. 7. Results of reaction of the ore fluid (1.3 kg) with host rock (100 g) at constant temperature (350 °C) in terms of (A) alteration minerals, (B) ore minerals (C) composition of the aqueous phase, (D) pH and oxygen fugacity. Mineral abbreviation after Kretz (1983): calcite (cal), chalcopyrite (ccp), diopside (di), epidote (ep), fluorite (fl), galena (gn), magnesium-chlorite (mg-chl), magnetite (mag), muscovite (ms), quartz (qtz), pyrrhotite (po), sphalerite (sp), talc (tlc), tremolite (tr).

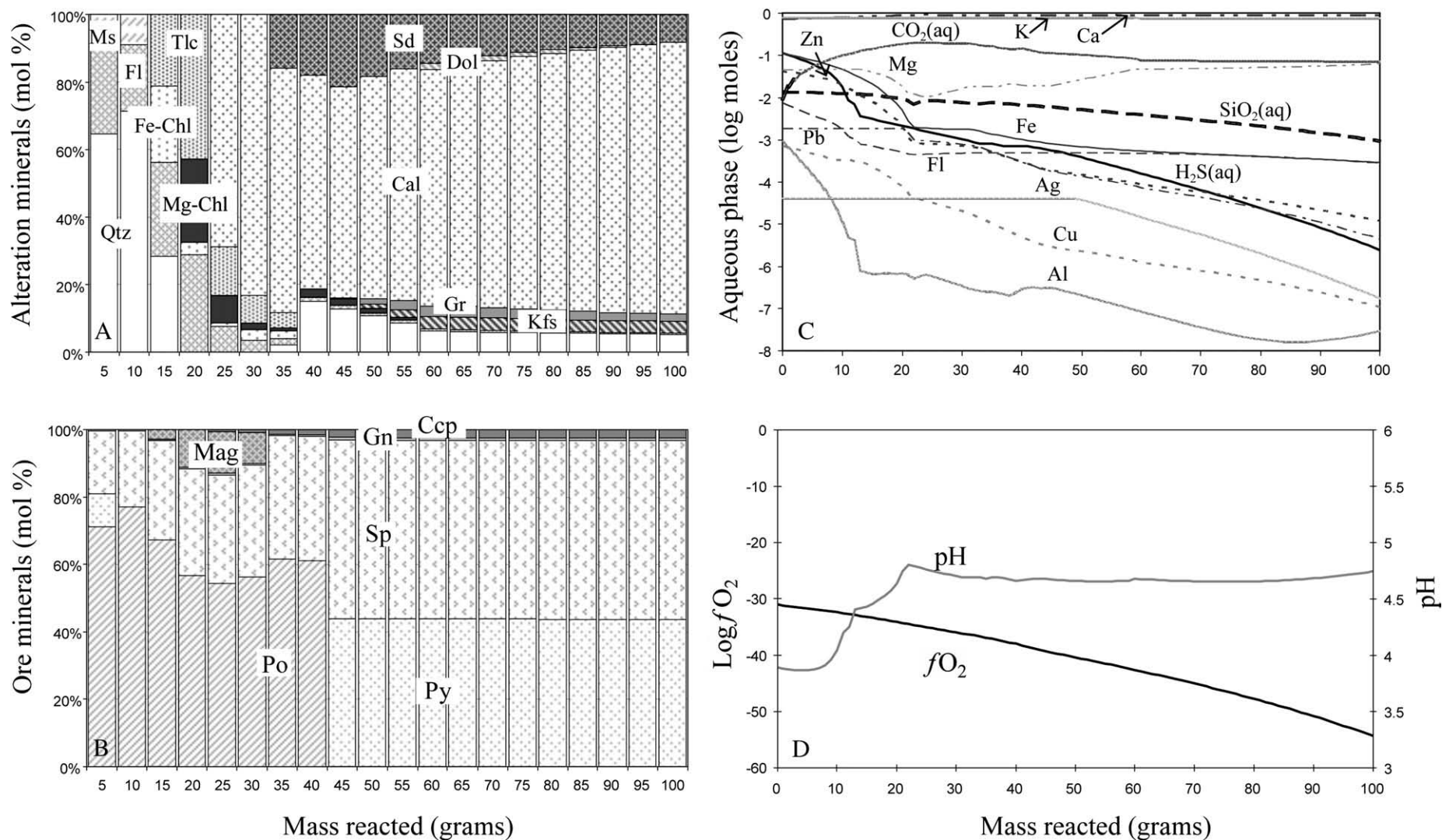


Fig. 8. Results of ore fluid- host rock interaction (1.3 kg–100 g) and cooling of the system from 350 °C to 100 °C. A) alteration minerals, (B) ore minerals (C) composition of the aqueous phase, (D) pH and oxygen fugacity. Mineral abbreviation after Kretz (1983): calcite (cal), chalcopyrite (ccp), dolomite (dol), ferroan-chlorite (fe-chl), fluorite (fl), galena (gn), graphite (gr), kfeldspars (kfs), magnesium-chlorite (mg-chl), magnetite (mag), muscovite (ms), quartz (qtz), pyrite (py), pyrrhotite (po), sphalerite (sp), siderite (sd), talc (tlc).

rock. It is an example of a titration model in which a fixed amount of rock is progressively added to the initial system. This type of model is useful to identify the series of reactions taking place when a rock reacts with fluid of a given composition, as well as recognize the type of alteration produced by the reactions. For our simulation of fluid–rock interaction we used 100 g of rock reacting with 1.3 kg of fluid. The composition of the rock has been reconstructed in order to be representative of the real composition of the host rock at Bismark and consists of 90% calcite, 5% quartz, 3% kaolinite and 2% clinocllore. The final process tested represents a combination of the previous two, i.e. fluid–rock interaction and simultaneous cooling.

6. Results

6.1. Temperature decrease

The predicted mineral assemblage from the cooling simulation includes three main stages (Fig. 6A): at higher temperature the system comprises quartz, pyrite, minor muscovite and fluorite ($T=350\text{--}320\text{ }^{\circ}\text{C}$), followed by a pyrite–quartz stage ($T=320\text{--}150\text{ }^{\circ}\text{C}$) and finally at lower temperature the mineral assemblages include sphalerite, pyrite and quartz with minor chalcopryrite (already present for $T<240\text{ }^{\circ}\text{C}$) and a little acanthite ($T\text{ }140\text{--}125\text{ }^{\circ}\text{C}$). Changes in the fluid composition comprise a decrease in the concentrations of $\text{SiO}_2(\text{aq})$, $\text{H}_2\text{S}(\text{aq})$, Cu, Zn and Fe due to the precipitation of quartz, chalcopryrite, sphalerite, pyrite and acanthite (not shown in Fig. 6A due to the very low amount precipitated; Fig. 6B). The oxygen fugacity of the system and the pH rapidly decrease from log -31 to log -61 and from 3.9 to 1.1 respectively due to the lack of any mineral to buffer the system (Fig. 6C).

6.2. Host rock reaction

The fluid–rock interaction at constant temperature and pressure ($T=350\text{ }^{\circ}\text{C}$, $P=200\text{ bar}$) initially precipitates pyrrhotite, sphalerite, quartz, muscovite and fluorite (Fig. 7A and B). As new rock is added to the fluid, quartz and muscovite are rapidly consumed and the initial stage minerals are replaced by the simultaneous precipitation of a sequence of skarn minerals and sulfides (Fig. 7A and B). Skarn minerals predicted include Mg-chlorite, talc, tremolite, diopside, epidote, and calcite. Development of skarn alteration is synchronous with the precipitation of ore minerals: pyrrhotite and sphalerite precipitate initially and further progression of the reaction yields a rapid increase in their amounts together with the precipitation of magnetite, galena and chalcopryrite (chalcopryrite is among the minerals that precipitate initially but is then redissolved in the fluid when less than 10 g of rock has reacted and then it precipitates again along with the other ore minerals; Fig. 7B). The sulfide precipitation is driven by an increase in the pH due to the reaction between the acidic fluid ($\text{pH}=3.9$) and the carbonate rock (Fig. 7D). The neutralization reaction consumes hydrogen forcing the pH to rise and consequently reducing the stability of Cl-complexes, leading to sulfide precipitation. The pH stops rising when calcite equilibrates with the fluid. Thus, one can consider the reaction completed when calcite precipitates for 23 g of rock reacted. The subsequent reaction produces a few changes that mainly consist of variations in the abundances of minerals. However, epidote is also precipitated and continuing reactions convert tremolite to diopside and diopside back to tremolite (Fig. 7B). The mineral assemblage when calcite first appears consists of pyrrhotite (45%), sphalerite (29.6%), magnetite (13%), tremolite (3.3%), clinocllore (2.9%), calcite (2.8%), fluorite (2.7%), galena (0.4%) and chalcopryrite (0.3%). Changes in the fluid composition reflect the evolution of the mineral assemblages during the reaction (Fig. 7C). The concentrations of Fe, Mg, Al, Zn, F, $\text{H}_2\text{S}(\text{aq})$, and $\text{SiO}_2(\text{aq})$ significantly decrease (more than one order of magnitude) in the interval 0–23 g of rock reacted due to the precipitation of ore and alteration minerals. The fluid is depleted by lesser amounts in Cu and Pb with concentrations decreasing less than one

order of magnitude due to the precipitation of chalcopryrite and galena respectively (Fig. 7C). In this interval the concentration of $\text{CO}_2(\text{aq})$ rapidly increases from 0.01 to 0.2 moles as shown in Fig. 7C as a result of calcite consumption to neutralize the fluid. After calcite equilibrates with the fluid there are no major further changes in the fluid composition, except an increase of aluminum, due to the dissolution of talc and the decrease of chlorite content, and a drop in the magnesium concentration caused by the precipitation of diopside (Fig. 7B and C).

6.3. Host rock reaction and cooling

The results of a fluid–host rock reaction with cooling are shown in Fig. 8A–D. For high fluid/rock ratio the resulting mineral assemblage consists mainly of pyrrhotite and sphalerite with pyrite, quartz and lesser muscovite and fluorite (Fig. 8A and B). As in the case of a fluid reacting with the host rock, the initial mineral assemblage is replaced at lower fluid/rock ratio and lower temperature by a series of skarn minerals and sulfides. Skarn minerals include talc, chlorite, and calcite (Fig. 8A). Sulfide minerals at this stage comprise abundant pyrrhotite, sphalerite, magnetite and lesser galena and chalcopryrite (Fig. 8B). Pyrite present in the initial stage is replaced by pyrrhotite (Fig. 8B). The precipitation of sulfide is again controlled by the increase in pH due to the neutralization of the acidic fluid (Fig. 8D). The pH stops increasing when calcite precipitates at 22 g of rock reacted. The mineral assemblage now consists of pyrrhotite (48.9%), sphalerite (28.9%), magnetite (11.6%), clinocllore (2.7%), fluorite (2.6%), tremolite (1.8%), talc (1.3%), calcite (1.1%) and chalcopryrite (0.5%). The fluid at this stage is depleted by more than one order of magnitude in Fe, Al, Zn, Cu, F and $\text{H}_2\text{S}(\text{aq})$ and to a lesser extent in Pb, Mg and $\text{SiO}_2(\text{aq})$ (Fig. 8C). By further adding rock mass to the fluid and lowering the temperature the reaction precipitates carbonates (siderite and dolomite), K-feldspar, quartz and graphite that leaves the fluid depleted in $\text{CO}_2(\text{aq})$, $\text{SiO}_2(\text{aq})$, Fe and K (Fig. 8A and C). Ore minerals in this late stage include abundant pyrite and sphalerite and lesser galena, chalcopryrite and acanthite. Pyrrhotite is no longer stable at lower temperature and is replaced by pyrite.

7. Discussion of modelling results and comparison with the Bismark ore stage minerals assemblage

The simulation of ore formation through just cooling process correctly predicts part of the assemblage observed at the Bismark deposit (Fig. 6A), however, the model does not produce pyrrhotite, galena and skarn minerals. The latter is expected, since there is no carbonate rock available. All these observations suggest that cooling alone was not responsible for skarn alteration and sulfide deposition, but was likely a contributing factor in the formation of the Bismark deposit.

The simulation of fluid–rock reaction reproduces with good approximation both ore and gangue minerals present at the Bismark deposit (Fig. 7A and B). The alteration minerals produced show a reasonably good correspondence with the skarn assemblage at Bismark, the only difference is the presence of tremolite instead of actinolite, but this is probably due to the inability of GWB to model solid solutions (Bethke, 1996, 2002). On the other hand the model predicts minerals not present at Bismark, such as epidote and talc. A complete skarn sequence comprises early anhydrous skarn followed by the precipitation of hydrous calc-silicates and sulfide. The model only predicts the formation of a hydrous skarn with anhydrous skarn represented by a small amount of pyroxene. The explanation is most likely the relatively low temperature ($350\text{ }^{\circ}\text{C}$) used in the calculation, because prograde skarn assemblages usually form at temperatures ranging from 650 to $400\text{ }^{\circ}\text{C}$ (Einaudi et al., 1981).

In terms of ore minerals, the simulation correctly predicts pyrrhotite, sphalerite, galena and chalcopryrite, but magnetite is not observed at the Bismark deposit. Relative abundances are also consistent to

those observed at Bismark with sphalerite more abundant than galena, however, the model fails to produce pyrite and silver. Sulfides precipitate during the first phases of the reaction in the interval 0–23 g of rock reacted with the fluid. In this interval the pH increased from 3.9 to 5.3, while the other parameters that may cause ore precipitation are constant (e.g. temperature, pressure and oxidation state; Fig. 7D). When calcite equilibrates with the fluid the pH stops increasing resulting in the cessation of sulfide precipitation. The abundance of sulfide does not significantly vary as the reaction continues. These observations suggest that the primary control on ore deposition was the pH increase due to the reaction between the fluid and the dominantly carbonate host rock. This is confirmed in the result of the last process tested. Simulation of fluid–rock reaction and simultaneous cooling presents a good prediction of ore and gangue minerals and offers the best matches between modelling results and the natural system (Fig. 8A and B). All the ore phases observed at the Bismark deposit are predicted by the model and their relative abundances are consistent with those of the deposit. Alteration minerals can be subdivided into two different stages; 1) at high temperature and high fluid/rock ratio the alteration assemblage is very similar to those produced for the simple reaction with the host rock (chlorite, talc, fluorite, tremolite and calcite); 2) at lower temperature and lower fluid/rock ratio these minerals are replaced (excluding calcite) by retrograde alteration phases siderite, dolomite, quartz, K-feldspar and graphite. Talc and graphite are not observed at Bismark, whereas K-feldspar is present during the early stages of skarn development. Finally, calcite, siderite and dolomite carbonates are present in the final phase of the ore stage. As in the previous process sulfide precipitated during the first phases of the reaction in the interval 0–22 g of rock reacted with the fluid. At this stage the temperature is still high (342 °C), while pH values increase from 3.9 to 4.9, providing further evidence that the primary control on ore deposition was the reaction with the carbonate host rock (Fig. 8D). Further progressing of the reaction leads to the precipitation of pyrite which replaced pyrrhotite (Fig. 8B). The pyrite–pyrrhotite transition is primarily controlled by temperature variations. The equilibrium between pyrite and pyrrhotite at constant temperature and pressure depends on the fO_2 , with pyrite and pyrrhotite stable at higher and lower fO_2 values respectively. As the temperature decrease, as it is the case here, the pyrite–pyrrhotite equilibrium shifts towards lower fO_2 values. The fO_2 decreases as the reaction progresses but not enough to stabilize pyrrhotite (Fig. 8D). This observation indicates that the temperature decrease was a key factor in controlling the precipitation of pyrrhotite first and its later transition to pyrite.

8. Conclusions

Geochemical modelling simulations allow to draw some important conclusions on the genesis of the Bismark deposit and some considerations on the behavior of zinc and lead in skarn deposits in general.

1. The modelling results indicate that ore deposition was the result of fluid neutralization caused by the reaction with the limestone host rock. This hypothesis is supported by the precipitation of sulfide in correspondence of the sudden increase of the pH in the first steps of the fluid–rock reaction. A temperature variation is likely to have contributed to ore deposition, particularly to the precipitation of pyrite, though simple fluid cooling was not the main mechanism that led to the formation of the Bismark deposit.
2. The trials, together with the analysis of the laser ablation data of ore stage fluid inclusions, also demonstrate that the amount of Zn and Pb precipitating from the ore fluid are dependent on the initial concentrations of Zn and Pb of the fluid.
3. Results from the modelling, in particular the close reproduction of ore stage minerals of the Bismark deposit, support the application

of fluid inclusion data to constrain geochemical modelling simulations as a valuable method to investigate geochemical processes.

Microanalytical results show excellent correlation between laser ablation and PIXE data for most inter-element ratios, although laser ablation provides a better estimate of the fluid composition due to its higher sensitivity compared to PIXE.

Acknowledgement

Work reported here was conducted as part of the predictive mineral discovery Cooperative Research Centre and this paper is published with the permission of the CEO, pmd*CR.

References

- Allan, M.M., et al., 2005. Validation of LA-ICP-MS fluid inclusion analysis with synthetic fluid inclusions. *American Mineralogist* 90 (11–12), 1767–1775.
- Baker, T., Lang, J.R., 2003. Reconciling fluid inclusion types, fluid processes, and fluid sources in skarns: an example from the Bismark Deposit, Mexico. *Mineralium Deposita* 38 (4), 474–495.
- Baker, T., van Achterberg, E., Ryan, C.G., Lang, J.R., 2004. Composition and evolution of ore fluids in a magmatic-hydrothermal skarn deposit. *Geology* 32 (2), 117–120.
- Bastrakov, E., 2003. Geoscience Australia Version of UNITERM Database for the HCh Package for Geochemical Modelling. Unpublished computer file. Available from author on request.
- Bastrakov, E., Shvarov, Y., Girvan, S., Cleverley, J., Wyborn, L., 2004. FreeGs: web-enabled thermodynamic database for modelling of geochemical processes. In: McPhie, J., McGoldrick, P. (Eds.), *Dynamic Earth: Past, Present and Future*, vol. 73. Abstracts – Geological Society of Australia, p. 52.
- Berman, R.G., 1988. Internally-consistent thermodynamic data for minerals in the system Na_2O – K_2O – CaO – MgO – FeO – Fe_2O_3 – Al_2O_3 – SiO_2 – TiO_2 – H_2O – CO_2 . *Journal of Petrology* 29 (2), 445–522.
- Bethke, C.M., 1996. *Geochemical reaction modeling: concepts and applications*. Oxford University Press, New York. 397 pp.
- Bethke, C.M., 2002. *The Geochemist's Workbench, Release 4.0*. University of Illinois, USA.
- Cleverley, J.S., Bastrakov, E.N., 2005. K2GWB: utility for generating thermodynamic data files for The Geochemist's Workbench(R) at 0–1000 °C and 1–5000 bar from UT2K and the UNITERM database. *Computers and Geosciences* 31 (6), 756–767.
- Eggins, S.M., Kinsley, L.P.J., Shelley, J.M.G., 1998. Deposition and element fractionation processes during atmospheric pressure laser sampling for analysis by ICP-MS. *Applications of Surface Science* 129, 278–286.
- Einaudi, M.T., Meinert, L.D., Newberry, R.J., 1981. Skarn deposits. In: Skinner, B.J. (Ed.), *Economic Geology seventy-fifth anniversary volume*. Society of Economic Geologists, Boulder, Colorado, pp. 317–391.
- Guillong, M., Gunther, D., 2002. Effect of particle size distribution on ICP-induced elemental fractionation in laser ablation-inductively coupled plasma-mass spectrometry. *Journal of Analytical Atomic Spectrometry* 17 (8), 831–837.
- Gunther, D., Heinrich, C.A., 1999. Comparison of the ablation behaviour of 266 nm Nd: YAG and 193 nm ArF excimer lasers for LA-ICP-MS analysis. *Journal of Analytical Atomic Spectrometry* 14 (9), 1369–1374.
- Gunther, D., Audetat, A., Frischknecht, R., Heinrich, C.A., 1998. Quantitative analysis of major, minor and trace elements in fluid inclusions using laser-ablation inductively-coupled-plasma mass-spectrometry. *Journal of Analytical Atomic Spectrometry* 13 (4), 263–270.
- Haptonstall, J.C., 1994. Bismark; Mexico's new major zinc mine. *Mining Engineering* 46 (4), 295–302.
- Heinrich, C.A., Ryan, C.G., Mernagh, T.P., Eadington, P.J., 1992. Segregation of ore metals between magmatic brine and vapor: a fluid inclusion study using PIXE microanalysis. *Economic Geology and the Bulletin of the Society of Economic Geologists* 87 (6), 1566–1583.
- Heinrich, C.A., Pettke, T., Halter, W.E., Aigner-Torres, M., Audetat, A., Gunther, D., Hattendorf, B., Bleiner, D., Guillong, M., Horn, I., 2003. Quantitative multi-element analysis of minerals, fluid and melt inclusions by laser-ablation inductively-coupled-plasma mass-spectrometry. *Geochimica et Cosmochimica Acta* 67 (18), 3473–3497.
- Heinrich, C.A., Driesner, T., Stefansson, A., Seward, T.M., 2004. Magmatic vapor contraction and the transport of gold from the porphyry environment to epithermal ore deposits. *Geology* 32 (9), 761–764.
- Helgeson, H.C., 1969. Thermodynamics of hydrothermal systems at elevated temperatures and pressures. *American Journal of Science* 267 (7), 729–804.
- Horn, I., Rudnick, R.L., McDonough, W.F., 2000. Precise elemental and isotope ratio determination by simultaneous solution nebulisation and laser ablation-ICP-MS: application to U–Pb geochronology. *Chemical Geology* 167 (3–4), 403–419.
- Kretz, R., 1983. Symbols for rock-forming minerals. *American Mineralogist* 68 (1–2), 277–279.
- Komninou, A., Sverjensky, D.A., 1995. Hydrothermal alteration and the chemistry of ore-forming fluids in an unconformity-type uranium deposit. *Geochimica et Cosmochimica Acta* 59 (13), 2709–2723.
- Komninou, A., Sverjensky, D.A., 1996. Geochemical modeling of the formation of an unconformity-type uranium deposit. *Economic Geology and the Bulletin of the Society of Economic Geologists* 91 (3), 590–606.

- Lu, C., Reed, M.H., Misra, K.C., 1992. Zinc-lead skarn mineralization at Tin Creek, Alaska: fluid inclusions and skarn-forming reactions. *Geochimica et Cosmochimica Acta* 56 (1), 109–119.
- Meinert, L.D., Hedenquist, J.W., Satoh, H., Matsuhisa, Y., 2003. Formation of anhydrous and hydrous skarn in Cu–Au ore deposits by magmatic fluids. *Economic Geology and the Bulletin of the Society of Economic Geologists* 98 (1), 147–156.
- Pokrovskii, V., Harrold, B., Heinrich, C., Liu, X., 1998. Release Notes for THERMADATA AGSO/ANU/ETH (version 5.2). Australian Geological Survey Organisation, Canberra.
- Ryan, C.G., Cousens, D.R., Heinrich, C.A., Griffin, W.L., Sie, S.H., Mernagh, T.P., 1991. Quantitative PIXE microanalysis of fluid inclusions based on a layered yield model. *Nuclear Instruments and Methods in Physics Research Section B: Beam Interactions with Materials and Atoms* 54 (1–3), 292–297.
- Ryan, C.G., Heinrich, C.A., Mernagh, T.P., 1993. PIXE microanalysis of fluid inclusions and its application to study of ore metal segregation between magmatic brine and vapor. *Nuclear Instruments and Methods in Physics Research v. B77*, 463–471.
- Ryan, C.G., Jamieson, D.N., Griffin, W.L., Cripps, G., Szymanski, R., 2001. The new CSIRO-GEMOC nuclear microprobe: First results, performance and recent applications. *Nuclear Instruments and Methods in Physics Research v. B181*, 12–19.
- Shinohara, H., Hedenquist, J.W., 1997. Constraints on magma degassing beneath the Far Southeast porphyry Cu–Au deposit, Philippines. *Journal of Petrology* 38 (12), 1741–1752.
- Shvarov, Y.V., Bastrakov, E.N., 1999. HCh: a software package for geochemical equilibrium modeling. User's guide. Australian Geological Survey Organisation, Record 1999/25.
- Sverjensky, D.A., 1987. The role of migrating oil field brines in the formation of sediment-hosted Cu-rich deposits. *Economic Geology and the Bulletin of the Society of Economic Geologists* 82 (5), 1130–1141.
- Ulrich, T., Gunther, D., Heinrich, C.A., 1999. Gold concentrations of magmatic brines and the metal budget of porphyry copper deposits. *Nature (London)* 399 (6737), 676–679.